1 # In situ [10]Be modeling and terrain analysis constrain subglacial
2 # quarrying and abrasion at Jakobshavn Isbræ, Greenland
3
4 Brandon L. Graham[1], Jason P. Briner[1], Nicolás E. Young[2], Allie Balter-Kennedy[2], Michele
5 Koppes[3], Joerg M. Schaefer[2], Kristin Poinar[1] and Elizabeth K. Thomas[1]
6
7 [1]Department of Geology, University at Buffalo, Buffalo NY USA
8 [2]Lamont-Doherty Earth Observatory, Columbia University, USA
9 [3]University of British Columbia, Vancouver, BC, Canada
10
11 *Correspondence to*: Jason P. Briner (jbriner@buffalo.edu)

12

13

14 **Abstract.** Glacial erosion creates diagnostic landscapes and vast amounts of sediment. Yet, knowledge about the

15 rate by which glaciers erode and sculpt bedrock and the proportion of quarried (plucked) versus abraded material is

16 limited. To address this, we quantify subglacial erosion rates and constrain the ratio of quarrying to abrasion during

17 the 19th/20th century overriding of a bedrock surface fronting Jakobshavn Isbræ, Greenland, by combining $^{10}$Be

18 analyses, a digital terrain model, and field observations. Cosmogenic $^{10}$Be measurements along a 1.2-m-tall quarried

19 bedrock step reveal a triangular wedge of quarried rock. Using individual $^{10}$Be measurements from abraded surfaces

20 across the study area, we derive an average abrasion rate of 0.13±0.08 mm yr$^{-1}$. By applying this analysis across a

21 ~1.33 km$^2$ study area, we estimate that the Greenland Ice Sheet quarried 378±45 m$^3$ and abraded 322±204 m$^3$ of

22 material at this site. These values result in an average total erosion rate of 0.26±0.16 mm yr$^{-1}$ with abrasion and

23 quarrying contributing in roughly equal proportions within uncertainty. Additional cosmogenic $^{10}$Be analysis and

24 surface texture mapping indicate that many lee steps are relict from the prior glaciation and were not re-quarried

25 during the recent overriding event. These new observations of glacier erosion in a recently exposed landscape

26 provide one of the first direct measurements of quarrying rates and indicate that quarrying accounts for roughly half

27 of total glacial erosion in representative continental shield lithologies.

28

29 **1. Introduction**

30     Distinctive features of glacier erosion characterize most glaciated regions, ranging from polished bedrock

31 surfaces to overdeepened fjords. Additionally, vast amounts of sediment are produced via glacial erosion. The

32 Greenland Ice Sheet accounts for a disproportionate delivery of sediment to the oceans, which impacts marine

33 ecosystems and carbon sequestration (e.g., Overeem et al., 2017). The two dominant mechanisms of glacier erosion

34 are subglacial quarrying and abrasion (Alley et al., 2019). Quarrying occurs when bedrock blocks are episodically

35 entrained and removed by overriding glaciers (e.g., Hallet, 1996; Iverson, 2012, Koppes, 2022). Abrasion occurs via

36 the gradual wearing down of bedrock surfaces as rock fragments are entrained and pressed into the bed by sliding

37 ice (Hallet, 1979; Iverson, 1990, Koppes, 2022). The rate at which each of these processes occur is dictated by rock

38 properties (e.g., Matthes, 1930; Dühnforth et al., 2010; Krabbendam and Glasser, 2011), glacio-hydraulic factors

39 (e.g., Egholm et al., 2012; Zoet et al., 2013; Anderson, 2014) and climate (e.g., Cook et al., 2020; Koppes 2022).

40 Although the result of the work done by glaciers on landscapes is dramatic, observational datasets that constrain

41 how quickly landscapes are modified by ice remain sparse (Alley et al., 2019).

42     Despite considerable challenges in observing erosional processes occurring under ice, our understanding of

43 subglacial erosion rates continues to expand. Total glacial erosion rates (i.e., abrasion + quarrying) have been

44 inferred using a variety of approaches (e.g., Hallet et al., 1996; Herman et al., 2021; Koppes, 2022) and are found to

45 generally fall between 0.01 and ≥1 mm yr$^{-1}$; however, higher rates have been measured on short (annual to decadal)

46 timescales (e.g., Koppes and Montgomery, 2009; Cowton et al., 2012). Attempts at separating the components of

47 quarrying and abrasion have been made based on sediment flux measurements (e.g., Loso et al., 2004; Riihimaki et

48 al., 2005), cosmogenic-nuclide inversions across subglacial bedforms (e.g., Briner and Swanson, 1998) and

49 theoretical considerations related to sparsely vs. intensely fractured bedrock (e.g., Anderson, 2014). To date,

50 measurements that isolate the eroded rock volume that can be attributed to quarrying are rare.

51      Here, we quantify subglacial erosion at a site that experienced a well constrained advance-retreat cycle of

52 Jakobshavn Isbræ, a major outlet glacier in West Greenland (Fig. 1). We partition total erosion into abrasion and

53 quarrying by pairing cosmogenic $^{10}Be$ measurements with analysis of a high-resolution terrain model and field

54 mapping of bedrock surface textures. We model the accumulation of cosmogenic $^{10}Be$ that we measured across a

55 quarried bedrock step to reconstruct the surface profile of the removed material, and the abrasion depth in adjacent

56 surfaces. Our data allow us to identify which bedrock steps experienced quarrying during the most recent advance of

57 the ice versus those unaltered since the prior glaciation. We thus calculate the volume of rock removed during the

58 recent overriding event by abrasion and by quarrying, and estimate the average erosion rate of each over the duration

59 of glacier overriding.

60

61 **2. Study area**

62      The north and south branches of Jakobshavn Isbræ merged and extended westward ~35 km within

63 Jakobshavn Isfjord to attain the "historical limit," which was observed in the fjord in 1850 CE (Fig. 1; Weidick and

64 Bennike, 2007). Adjacent to Jakobshavn Isfjord, the historical limit is represented by a prominent moraine

65 demarcating the extent of the "historical advance," which more or less coincides with the Little Ice Age. Prior

66 authors calculated (1) the timing of deglaciation following the last glacial maximum to the historical limit at 7500 yr

67 ago (Young et al., 2011; Balter-Kennedy et al., 201) and to the present ice position by 7400 yr ago, and (2) the

68 advance (~1790 CE) and retreat (2010 AD; a duration of 220±5 yr) of Jakobshavn Isbræ at the study site (Briner et

69 al., 2011; Young et al. 2016; Balter-Kennedy et al., 2021; Fig. 1). It is thought that Jakobshavn Isbræ receded during

70 the Holocene deglaciation to a position ~20 km inland of the present ice margin (Weidick et al., 1990; Kajanto et al.,

71 2020). Our study builds on Young et al. (2016) and Balter-Kennedy et al. (2021), who utilized cosmogenic $^{10}Be$

72 measurements to quantify total subglacial erosion rates of the gneissic bedrock in this area (Fig. 1).

73

74 **3. Methods**

75      In August 2018, we investigated a bedrock forefield adjacent to the north branch of Jakobshavn Isbræ that

76 emerged from beneath the ice between 2008 and 2010 based on available satellite imagery (Balter-Kennedy et al.,

77 2021). The surface of glacially abraded and quarried bedrock exhibits pristine features of glacial erosion (Fig. 2).

78 We measured ice-flow orientations, noted rock surface texture (variations in texture are accompanied by tonal

79 differences in the color of rock surfaces), used drone imagery to generate a high-resolution digital terrain model, and

80 collected samples for cosmogenic $^{10}Be$ measurements.

81      Two stoss and lee landforms were chosen for detailed cosmogenic $^{10}Be$ analysis, with the goal of

82 characterizing quarrying volume and timing. We chose one landform (Location A; Fig. 3A) to (1) estimate the

83 dimensions of the bedrock removed based on the geometry of a quarried divot, where there is a sharp transition from

84 rough to abraded surface texture surrounding the quarried zone, and (2) use $^{10}Be$ concentrations in samples collected

85 from the quarried divot to reconstruct the profile of the pre-quarried surface. We created a 3D forward model of

86    cosmogenic [10]Be production to estimate the shape of the quarried material (single or multiple blocks) at location A.

87    The fundamental set-up of our conceptual model is shown in Figure 4. At another site (Location B; Fig. 3B), where

88    two adjacent lee steps have different surface textures, we measured the [10]Be concentration at the base of each step to

89    test our hypothesis that the variations in surface texture relate to quarrying during the historical overriding versus the

90    prior glaciation.

91

92    **3.1 Field sampling for [10]Be analysis**

93    At Location A, we nearly continuously sampled every ~5 cm from the top of the vertical face (0 cm, at the edge of

94    the stoss surface) to 69 cm depth, then we skipped down to sample the base of the lee face at 115 cm. We measured

95    [10]Be concentrations in five samples on the lee face: the top of the lee cliff ("surface"), from 12-15 cm, 30-33 cm, 65-

96    69 cm and 110-115 cm at the base. Wide, thin samples were collected (30 cm W x 3-5 cm H x 2-4 cm D) to

97    optimize the quartz mass within a narrow depth range and to minimize depth integration. We also collected three

98    samples along the horizontal floor, two from within the quarried scar and one beyond the distal edge of the quarried

99    scar from a polished surface (Fig. 3). At Location B, we collected one sample from the base of the lee cliff from

100   each zone (Fig. 3). All samples were collected with a combination of Hilti brand angle grinder with 5-inch diameter

101   diamond bit blades, and hammer and chisel. At all sampling locations, field observations of topographic shielding

102   were collected using a Brunton compass. Location and elevation were collected with a GPS time averaging smart

103   phone application with ±5 m accuracy.

104

105   **3.2 Terrain analysis and surface textures**

106   Aerial imagery was collected with a DJI Mavic Pro unmanned aerial vehicle (UAV) with continuous and

107   overlapping nadir imagery acquired using DJI smartphone app software. Maps Made Easy

108   (www.mapsmadeeasy.com; last access: April 26, 2023) was used to generate orthoimagery and a digital elevation

109   model (DEM) of the field area using structure from motion principles (Graham, 2023). Mosaic imagery was used as

110   a base layer for field mapping three surface roughness categories of the stoss and lee landforms based on the degree

111   of freshness (1: freshly exposed surfaces with minor grain-to-grain relief and no apparent abrasion, 2: lightly

112   abraded, 3: heavily abraded and polished). We also observed that the fresh-appearing surfaces exhibited darker

113   surface colors, and that smoother surface textures exhibited lighter surface colors. The orientation of ice flow

114   indicators consisting of striae, gouges, chatter marks, and crescentic gouges were measured using a compass.

115

116   **3.3 Beryllium-10 Laboratory Methods**

117   All physical rock processing and isolation of quartz for [10]Be analysis was performed at the University at Buffalo

118   Cosmogenic Isotope Laboratory (Corbett et al., 2016; Kohl & Nishiizumi, 1992). Pure quartz was processed at the

119   Lamont-Doherty Earth Observatory cosmogenic dating laboratory following established beryllium extraction

120   procedures. We processed eight samples from Location A, and two samples from Location B. AMS measurements

121   of [10]Be/[9]Be were performed at the Center for Accelerator Mass Spectrometry at Lawrence Livermore National

122   Laboratory (LLNL-CAMS), with references relative to the 07KNSTD standard of known [10]Be/[9]Be ratio of 2.85 x

123  $10^{-12}$ (Nishiizumi et al., 2007). Measured 1σ analytical uncertainty ranged from 1.77% to 3.43% (Table S1).

124  Apparent exposure ages were calculated using the online cosmogenic age calculator v3 (Balco et al., 2008) using the

125  Baffin Bay [10]Be production rate calibration data set (Balco et al., 2008; Young et al., 2013). Apparent exposure age

126  refers to the calculated age if the samples were at the surface and experienced zero erosion. Although these apparent

127  ages are not used in our erosion models, they are instructive in analyzing and visualizing the context of the data

128  based on a priori assumptions.

129

130  **3.4 Cosmogenic Nuclide Modeling**

131  Following Balco et al. (2011), we created a 3D forward model (Graham, 2023) of cosmogenic [10]Be production in the

132  upper 1.2 meters of the glacially eroded bedrock at Location A using the known exposure and burial history. The

133  history we adopt is shown in Fig. 4 and is as follows: Exposure from 7400 years ago to 1790 CE (~7200 years of

134  exposure), burial from 1790 to 2010 CE (220 years of burial/erosion), and exposure from 2011 to 2018 CE (year of

135  sample collection). We use the model to not only quantify the pre-quarrying surface, but also to determine the

136  sensitivity of the specific sampling locations in the resulting divot. We thus prioritized certain sample locations from

137  the vertical (lee) face to optimize the number of samples measured. To start, we simulated the [10]Be concentrations

138  using a variety of pre-quarrying surface shape geometries ranging from a rectangular cross section to a triangular

139  cross section to a geometry that is the same as the present-day surface. End members of these pre-quarrying surface

140  options are illustrated as the purple, green and red lines in Figure 5B. Three-dimensional representations were

141  generated by extending the 2D surface profiles laterally. This simplified the hypothetical surface models and was

142  justified by the presence of laterally similar surface profiles observed on the landscape. Simulated cosmic particle

143  bombardment was prescribed based on Gosse and Phillips (2001) for azimuth and elevation angles through the

144  simulated overlaying bedrock to each sample location.

145      We next created an inverse model to solve for the pre-quarrying surface profile at Location A. An adaptive

146  Metropolis Hastings Markov Chain Monte Carlo (MCMC) Matlab solver package (Haario et al., 2006) was

147  implemented to estimate the parameters necessary to minimize the chi-squared reduction of the estimated [10]Be

148  concentrations to the measured [10]Be concentrations. The unknown parameters were: 1) the surface profile x

149  (horizontal distance within the quarried block) inflection point, 2) the surface profile z (depth) inflection point, 3)

150  the depth of surface abrasion applied equally across all samples, and 4) the absolute attenuation length ($\Lambda_{abs}$) of the

151  high energy neutron spallation through the rock. Acceptable a priori parameter ranges were initially prescribed

152  (Table 1). We used the MCMC inversion to solve for the posterior parameters that correspond to the minimized [10]Be

153  concentrations through the chi squared reduction. Due to the relatively shallow maximum sample depth (~1.2

154  meters) and small amount of abrasion previously estimated by Balter-Kennedy et al. (2021), muon production is

155  minimal and approximately linear across the narrow depth range. Therefore, we treated production via muons as a

156  linear function of depth across all sample sites.

157      The surface profile was generated via a point with X,Z coordinates located within the pre-quarrying

158  geometries prescribed above. To expand laterally, a 25-point smoothed surface interpolation (Matlab function pchip)

159  was applied between the generated point and the edges of the quarried block (top of the stoss cliff, and the rough-to-

160  smooth transition around the perimeter of the quarried block). The initial estimate of abrasion depth for the model is

161  based on an abrasion depth estimate from the surface sample 18JAK-Surface following the methods described in

162  Briner and Swanson (1998) and Young et al. (2016) and is independent (but complementary) to results obtained by

163  Balter-Kennedy et al. (2021). The absolute attenuation length ($\Lambda$abs) is based on the range of values estimated in

164  Gosse and Phillips (2001). Most estimations of spallation attenuation with depth rely on the apparent attenuation

165  length ($\Lambda$app) because it assumes a horizontally infinite half space, or a flat surface profile, which the sample lays

166  beneath at some depth, z (cm). Due to the off-zenith incoming cosmic particles travelling through an increasing

167  length of mass, an integrated value of attenuation results in the apparent attenuation (Dunai, 2010). Because our

168  research incorporates a complex surface model, the absolute attenuation length is required to properly simulate the

169  attenuation through varying thicknesses of rock from off-zenith angles. Our inversion results in an estimate for an

170  absolute attenuation length of $184\pm13$ g cm$^{-2}$. When converted to an apparent attenuation length, via $\Lambda$app =

171  $(3.3/4.3)*\Lambda$abs, this becomes $141\pm10$ g cm$^{-2}$ and is within the range reported for the Arctic by Gosse and Phillips

172  (2001).

173

174  **3.5 Terrain analysis and volume of quarried material**

175  We applied the resulting most probable profile of the quarried block at Location A (see Results) to other divots that

176  were quarried during the historical advance. Incidentally, the shape of the quarried material is consistent with, and

177  could largely be defined by, the non-quarried surfaces surrounding the quarried divots. Informed by results from the

178  cosmogenic nuclide measurements at Location B and surface texture mapping, we identified which of the quarried

179  divots were excavated during the historical advance versus glacier overriding associated with the last glaciation. The

180  latter quarried zones were excluded from the analysis to prevent overestimating the quarried rock volume attributed

181  to the historical overriding event. All geographical information system (GIS) analysis was performed in QGIS

182  Desktop 3.16 Long Term Release, with all datasets transformed to NSIDC Sea Ice Polar Stereographic North. The

183  UAV-generated DEM, nominally 0.03 m raster cell size after transformation, was re-gridded to 0.05 m cell size to

184  which all further raster analysis was standardized to. We defined our field area based on the extent of an

185  exceptionally bedrock-rich part of the glacier forefield, with a higher degree of surface sediment cover around its

186  periphery. Some areas of sediment cover from within our outlined study zone are excluded because they occluded

187  accurate identification of the underlying surface texture and are not included in area calculations of the study site.

188      We defined the quarried zones attributed to the historical advance with polygons and removed them from

189  the DEM of the present-day surface. We then interpolated a synthetic surface across the missing holes in the DEM

190  to recreate the pre-1790 CE surface, or "paleo-surface" using the geometry guided by results from Location A. Next,

191  we generated a difference map between the paleo-surface DEM and the present-day surface DEM. We then summed

192  these values from the difference map. Finally, when applying the resultant abrasion rate across the study area, we

193  estimated a cavity area below each of the historically quarried zones (assuming a seasonally averaged cavity roof of

194  45°) and subtracted this area from the total study area.

195

### 4. Results

196

197   The $^{10}$Be concentrations from Location A (Table 2) decrease with depth and increase along the floor

198 outwards from the lee cliff base (Fig. 5B). All samples result in lower apparent exposure ages than the estimated

199 exposure duration of 7200 yr (7400 yr deglaciation minus 200 yr of subsequent burial), indicating that glacial

200 erosion recently took place. The best fit of our forward model is a triangular wedge shape of removed material (Fig.

201 5B & C, green). This shape is supported by the surface morphology and textures adjacent to the quarried divot.

202 Furthermore, this triangular wedge shape is supported by the MCMC model, which reveals a slightly concave pre-

203 quarried block surface (see "MCMC" in Fig. 5B). Additionally, our MCMC modelling using all samples at Location

204 A yielded a surface abrasion depth of 4.1±1.9 cm (Table 1). When using individual samples from the top (stoss) side

205 of the lee ledge and from beyond the quarried divot, we derive abrasion depths of 2.7±1.1 and 5.8±1.1 cm,

206 respectively.

207   To estimate an abraded volume of the study site, we consider several distinct abrasion rates calculated

208 across the study area. Combining abrasion depths mentioned above with four nearby values reported by Balter-

209 Kennedy et al. (2021) yields an average abrasion depth of 2.78±1.84 cm and an abrasion rate of 0.126±0.084 mm

210 yr$^{-1}$. Calculating the volume of material abraded requires the removal of areas where cavities existed in the

211 immediate lee of bedrock steps. Although cavities change in size seasonally, we estimate that 12% of the field area

212 consists of cavities assuming a 45° sloping cavity roof from the lip of bedrock steps. We thus calculate a volume of

213 322±204 m$^3$.

214   Results from Location B show significant differences in the measured $^{10}$Be concentrations between the two

215 lee steps. Sample ER2-A was collected at the base of an 85-cm-tall lee face that exhibits a fresh (non-polished)

216 surface texture and a darker color (Fig. 3C). Its apparent exposure age of 2.3 ka (accounting for shielding using

217 present topography) is significantly less than the expected age of ~7.2 ka, indicating quarrying during the historical

218 advance over the site. Sample ER2-B is from the base of a 120-cm-tall lee cliff and exhibits a lightly abraded texture

219 and lighter color (Fig. 3B). Its apparent exposure age when accounting for shielding using present topography is 6.9

220 ka. We attribute the difference in apparent age of sample ER2-B and its expected age of 7.2 ka to a few centimeters

221 of abrasion, and more importantly, to a lack of quarrying during the historical advance. Thus, the results from

222 Location B indicate that other bedrock steps that exhibit smoother, lightly abraded surfaces were quarried during the

223 prior glaciation, and that only rougher, darker-colored surfaces in some lee faces were quarried during the historical

224 advance.

225   Our field mapping of rock surface textures exhibits quarried zones with a mixture of rough and abraded lee

226 surfaces. We identified 73 quarried zones classified with rough-textured, dark-colored surfaces ("historical"

227 quarrying) and 84 quarried zones classified as having slight smoothing and lighter surface tone (quarrying during the

228 last glaciation; Fig. 6). We calculate an area of quarried material during the historical advance of 1,635–2,050 m$^2$

229 (the derivation of this range is discussed below) of the total 13,256 m$^2$ field area (12–15%) and a quarried volume of

230 378±45 m$^3$. Using the duration of overriding during the historical advance, this equates to an equivalent quarrying

231 rate of 0.13±0.03 mm yr$^{-1}$ when averaged across the study site. We calculate a combined (total) eroded rock volume

232 of 700±249 m$^3$ and total subglacial erosion rate of 0.26±0.16 mm yr$^{-1}$, of which 47% is attributed to abrasion and

233 53% is attributed to quarrying.

234        Measurements of ice flow indicators, including striations, crescentic gouges and chatter marks, reveal a

235 south (180°) to southwest (225°) ice-flow direction (Fig. 7). When sorted by type of ice flow indicator, a pattern

236 emerges showing an evolution of flow direction during the most recent ice advance. Small striations, being the most

237 likely to represent the final ice-flow direction before deglaciation, show the most recent ice flow direction toward

238 the south. Crescentic gouges, chatter marks and lee face orientations, which are more likely to persist after some

239 surface abrasion, reveal a southwesterly direction of ice flow. This shift likely represents the evolving flow direction

240 and velocity change as ice flow over the field area increased in velocity, shifted to the southwest and thickened

241 during the maximum phase of the historical advance. Based on the orientation of quarrying ledges and ice flow

242 indicators, it thus appears that much of the quarrying occurred when the ice flowed southwest during what was

243 presumably the highest ice flow velocity and thickness of the historical advance.

244

245 **5. Discussion**

246        We provide a new approach for quantifying the quarried volume of sediment across a glacial landscape and

247 for partitioning the relative contributions of quarrying and abrasion. Due to the inherent difficulty in measuring

248 quarrying directly, previous estimates rely on computational models or inferences made from measurements of

249 proglacial sediment discharge (Hallet, 1996; Loso et al., 2004; Riihimaki et al., 2005; Ugelvig et al., 2018).

250 Quarrying estimates from stream sediments (e.g., bedload) require assumptions about the portion of the suspended

251 load that is also derived from quarrying (Riihimaki et al., 2005). Here, our measurements of quarrying volume and

252 rate stem from the combination of in situ $^{10}$Be measurements and terrain analysis.

253        Our erosion rate measurements are similar to other estimates for glacial erosion in Greenland and beyond

254 (Koppes and Montgomery, 2009; Cook et al., 2020). Our total erosion rate of 0.32±0.09 mm yr$^{-1}$ is similar to what

255 Balter-Kennedy et al. (2021) found at the same site using both surface $^{10}$Be measurements (0.4–0.8 mm yr$^{-1}$) and a

256 $^{10}$Be depth profile from a 4-m-deep rock core (0.3–0.6 mm yr$^{-1}$). Although these rates are lower than those found

257 using a sediment-budget approach in southwestern Greenland (4.8±2.6 mm yr$^{-1}$; Cowton et al., 2012), they are

258 similar to centennial-scale erosion rate estimates of 0.29–0.34 mm yr$^{-1}$ in northwestern Greenland (Hogan et al.,

259 2020).

260        Quarrying is inferred to be highly dependent on glaciological and lithological conditions, including bedrock

261 hardness and fracture spacing (Dühnforth et al., 2010; Krabbendam and Glasser, 2011; Iverson, 2012). Our study

262 site contains competent, hard crystalline rock with widely spaced fractures (on the order of several meters). Thus,

263 based on these characteristics, we would expect abrasion to dominate at our field site (Anderson, 2014). However,

264 despite only 12–15% of the field site by area exhibiting recent quarrying, we calculate that 53% of total glacial

265 erosion occurred as quarrying.

266        Our MCMC results and field observations suggest that, prior to quarrying, the bedrock surface was

267 relatively low relief, likely with wave cavities in lee locations (Zoet et al., 2013) as opposed to stepped geometries

268 that are more often considered in theoretical studies of quarrying (e.g., Anderson et al., 1982; Hallet, 1996; Iverson,

269    2012; Anderson, 2014). Despite bedrock characteristics inhibiting quarrying, the Greenland Ice Sheet experiences

270    significant seasonal and sub-seasonal changes in subglacial hydrology in this area (Das et al., 2008; Andrews et al.,

271    2014), which is thought to aid quarrying processes (Anderson, 2014; Ugelvig et al., 2018). Propagating fractures that

272    are presumed to eventually lead to failure and quarrying appear to not solely rely on pre-existing fractures in the

273    bedrock at our study site, but could have been induced from processes related to the formation of crescentic gouges

274    (Gilbert, 1905) that we observed in abundance in the field (Fig. 2A). That many crescentic gouge trains increase in

275    size toward quarried ledges–with a crescentic gouge at the lip of many edges–may indicate that gouge formation is a

276    fracture nucleation point that leads to quarrying events in this field area (Figs. 2 and 8).

277            There are uncertainties associated with calculating erosion depth, volume and rate. We do not expect

278    uniform abrasion across the study area given the stepped nature of the terrain and localized variations in basal stress.

279    At Site A, we find a lower abrasion depth at the lip of the divot (2.7±1.1 cm) than the floor beyond the quarried zone

280    (5.8±1.0 cm). We do not have enough data to elucidate predictable spatial patterns of more or less abrasion across

281    the study site; instead, we rely on an average of a number of data points that provide a useful representative abrasion

282    depth to apply across our field area.

283            It is useful to further consider uncertainties, such as those perhaps associated with our erosion thickness,

284    volume and rate results. Abrasion depth estimates reported here have high uncertainty due to the inherent

285    measurement error in measuring cosmogenic nuclide concentration. An analysis of errors in Young et al. (2016) and

286    Balter-Kennedy et al. (2021) for shallow abrasion depths shows a consistently appreciable uncertainty in relation to

287    the low magnitudes of rock removal via abrasion. The measurement uncertainties for samples in the companion

288    study of Balter-Kennedy et al. (2021) is ∼2.5–3 cm, but when the estimated depth of abrasion is small and similar to

289    mean uncertainty, the uncertainty can result in a significant range of the abraded depth. One advantage of our

290    experiment at Location A is that multiple samples were used in the MCMC inversion, reducing the uncertainty in the

291    estimated abrasion depth. Unfortunately, even with the added resolving power of multiple samples, the uncertainty

292    in the abrasion depth is still 46%.

293            When converting the abrasion depth to an abrasion rate, another source of uncertainty is the duration of

294    erosion. Whereas the timing of recent deglaciation and exposure is well constrained, the timing of burial is less well

295    constrained. We use the overriding duration of 1790–2010 CE used in Balter-Kennedy et al. (2021), which is based

296    on prior work in the area (Briner et al., 2011; Young et al., 2016). Although we use an absolute date range in our

297    erosion rate calculations, the initiation glaciation at the onset of the historical advance at our study site is

298    reconstructed, not observed, and the initiation timing of overriding would affect the calculated erosion rates. If the

299    ice arrived decades earlier (we think this is more likely than ice arriving later than 1800 CE), our calculated erosion

300    rates would decrease, but the ratio of abrasion to quarrying would be unaffected.

301            An additional source of uncertainty relates to the reconstructed profile of the paleo-surface slope of

302    quarried blocks, and thus of the volume of each removed block. We use the three-dimensional nuclide production

303    inversion of the quarried zone at Location A to guide the shape for other quarried zones. To estimate the uncertainty

304    of each quarried block, and the cumulative uncertainty of the quarried volume across the study site, each zone was

305    analyzed for the likelihood of having a pre-quarrying sloped, triangular profile versus a more rectangular, stair-step

306    profile. Of the 73 quarried zones, 63 were identified as triangular shape based on the localized topography around

307    each quarried zone, as was the case at Location A that we confirmed with our cosmogenic nuclide measurements

308    and modeling. The remaining 10 locations were identified as likely to have been rectangular blocks, and the rock

309    volume quarried at these sites was calculated by doubling the volume generated by a triangular cross-section.

310        The uncertainty in our estimates of quarried rock volume is independent of the cosmogenic nuclide

311    concentration. To estimate uncertainty in our manual outlining of each area of the quarried zones, a 0.5-meter buffer

312    was extended at the edge of the floor of each quarried zone; this edge is based on changes in surface texture from

313    rough to smooth as recorded in the high-resolution orthoimagery. The location of this transition is also dictated by

314    the presence/absence of chatter marks/crescentic gouges, surface patina, and rock color. While many locations have

315    a well-defined transition, 0.5 meters is an upper limit on our ability to define this boundary. The lee cliff is a well-

316    defined feature on the landscape, and is accurately identified from the orthoimagery, with assistance using other

317    products such as the DEM, and Hillshade/Roughness QGIS processing products. We consider our 0.5 m buffer on

318    the extent along the quarried floor to be a conservative estimate. When used to define the volume of each block, we

319    find that the 0.5 m buffer equates to a volume range of $379\pm45$ m$^3$, and a quarried area of $1842\pm100$ m$^2$ (12–15% of

320    the study area).

321        Our inverse modeling of cosmogenic nuclide production at Location A highlights the continued importance

322    of cosmogenic nuclides in glacier erosion studies. Optimizing sampling locations to estimate the parameters of

323    interest (surface geometry of a removed block, depth of abrasion, and attenuation length) was important for our

324    inversion results. The sensitivity analysis to determine how samples were important in our forward model scenarios

325    aided in sample selection for processing. The samples along the horizontal lee floor (FL1, FL2) are the most

326    important for constraining the surface profile shape. Samples at the present-day surfaces (Surface, FL3) are the most

327    important for constraining the depth of abrasion, while the samples collected along the vertical lee cliff are sensitive

328    to the depth of abrasion and the attenuation length. In fact, not all samples collected along the vertical cliff were

329    needed for the analysis, while additional samples along the floor near the quarrying-abrasion transition could have

330    been beneficial.

331

332    **6. Conclusion**

333        Our pairing of cosmogenic nuclide analysis with inverse modeling of cosmogenic nuclide

334    production through quarried material, along with topographic and morphologic analysis of a recently deglaciated

335    bedrock landscape, provides one of the first direct observation-based estimates of glacial quarrying and partitioning

336    of glacial erosion processes. We found that quarried volume generally matched that of abrasion despite a hard

337    crystalline bedrock with wide fracture spacing and a low-relief surface morphology, all conspiring to limit

338    quarrying. It seems that quarrying mostly took place via triangular wedge removal at this site. Field observations

339    suggest clast-bed impacts evidenced by abundant crescentic gouges are a possible mechanism to nucleate quarrying

340    events, assisted by seasonal and sub-seasonal fluctuations in subglacial water pressure. These results are a small

341    addition to a field that needs further analysis. Yet, field data like these are important for grounding landscape

342    evolution models with observational datasets and for providing fundamental information for understanding coupled

343    glacier-hydrology-sediment production processes. Ultimately, the results of our work invite further analysis at this

344    field site, including testing of both theoretical and computational models of glacial erosion.

345

346    **Code and data availability**

347    Code and data are available on GitHub at https://github.com/w0gpr/Cosmo3D (last access: April 26, 2023) and

348    Zenodo (https://doi.org/10.5281/ZENODO.7858913; Graham, 2023).

349

350    **Author contribution**

351    BG, JPB, NEY and AB-K designed the study and collected field data. BLG, JPB and JMS led rock sample

352    preparation and [10]Be analysis. BG modeled [10]Be production, computed terrain analysis, and derived erosion results.

353    MK, KP and EKT provided significant input throughout the course of this research. BG and JPB prepared the paper

354    with contributions from all co-authors.

355

356    **Competing Interests**

357    The contact author declares that none of the authors have any competing interests. Kristin Poinar is a member of the

358    editorial board of The Cryosophere

359

367

368    **References**

369

370    Alley, R. B., Cuffey, K. M., and Zoet, L. K.: Glacial erosion: status and outlook, Ann. Glaciol., 60, 1–13,

371    https://doi.org/10.1017/aog.2019.38, 2019.

372

373    Anderson, R. S.: Evolution of lumpy glacial landscapes, Geology, 42, 679–682, https://doi.org/10.1130/G35537.1,

374    2014.

375

376    Anderson, R. S., Hallet, B., Walder, J., and Aubry, B. F.: Observations in a cavity beneath grinnell glacier, Earth

377    Surf. Process. Landforms, 7, 63–70, https://doi.org/10.1002/esp.3290070108, 1982.

378

379  Andrews, L. C., Catania, G. A., Hoffman, M. J., Gulley, J. D., Lüthi, M. P., Ryser, C., Hawley, R. L., and Neumann,
380  T. A.: Direct observations of evolving subglacial drainage beneath the Greenland Ice Sheet, Nature, 514, 80–83,
381  https://doi.org/10.1038/nature13796, 2014.
382
383  Balter-Kennedy, A., Young, N. E., Briner, J. P., Graham, B. L., and Schaefer, J. M.: Centennial- and Orbital-Scale
384  Erosion Beneath the Greenland Ice Sheet Near Jakobshavn Isbræ, JGR Earth Surface, 126,
385  https://doi.org/10.1029/2021JF006429, 2021.
386
387  Bernard, H.: A Theoretical Model of Glacial Abrasion, J. Glaciol., 23, 39–50,
388  https://doi.org/10.3189/S0022143000029725, 1979.
389
390  Briner, J. P. and Swanson, T. W.: Using inherited cosmogenic 36Cl to constrain glacial erosion rates of the
391  Cordilleran ice sheet, Geol, 26, 3, https://doi.org/10.1130/0091-7613(1998)026<0003:UICCTC>2.3.CO;2, 1998.
392
393  Briner, J. P., Young, N. E., Thomas, E. K., Stewart, H. A. M., Losee, S., and Truex, S.: Varve and radiocarbon
394  dating support the rapid advance of Jakobshavn Isbræ during the Little Ice Age, Quaternary Science Reviews, 30,
395  2476–2486, https://doi.org/10.1016/j.quascirev.2011.05.017, 2011.
396
397  Cook, S. J., Swift, D. A., Kirkbride, M. P., Knight, P. G., and Waller, R. I.: The empirical basis for modelling glacial
398  erosion rates, Nat Commun, 11, 759, https://doi.org/10.1038/s41467-020-14583-8, 2020.
399
400  Cowton, T., Nienow, P., Bartholomew, I., Sole, A., and Mair, D.: Rapid erosion beneath the Greenland ice sheet,
401  Geology, 40, 343–346, https://doi.org/10.1130/G32687.1, 2012.
402
403  Das, S. B., Joughin, I., Behn, M. D., Howat, I. M., King, M. A., Lizarralde, D., and Bhatia, M. P.: Fracture
404  Propagation to the Base of the Greenland Ice Sheet During Supraglacial Lake Drainage, Science, 320, 778–781,
405  https://doi.org/10.1126/science.1153360, 2008.
406
407  Dühnforth, M., Anderson, R. S., Ward, D., and Stock, G. M.: Bedrock fracture control of glacial erosion processes
408  and rates, Geology, 38, 423–426, https://doi.org/10.1130/G30576.1, 2010.
409
410  Dunai, T. J.: Cosmogenic Nuclides: Principles, Concepts and Applications in the Earth Surface Sciences, 1st ed.,
411  Cambridge University Press, https://doi.org/10.1017/CBO9780511804519, 2010.
412
413  Egholm, D. L., Pedersen, V. K., Knudsen, M. F., and Larsen, N. K.: Coupling the flow of ice, water, and sediment in
414  a glacial landscape evolution model, Geomorphology, 141–142, 47–66,
415  https://doi.org/10.1016/j.geomorph.2011.12.019, 2012.

416

417 Gilbert, G. K.: Crescentic gouges on glaciated surfaces, Geological Society of America Bulletin, 17, 303–316,

418 https://doi.org/10.1130/GSAB-17-303, 1906.

419

420 Gosse, J. C. and Phillips, F. M.: Terrestrial in situ cosmogenic nuclides: theory and application, Quaternary Science

421 Reviews, 20, 1475–1560, https://doi.org/10.1016/S0277-3791(00)00171-2, 2001.

422

423 Graham, B.: w0gpr/Cosmo3D: v1.0.0, https://doi.org/10.5281/ZENODO.7858913, 2023.

424

425 Haario, H., Laine, M., Mira, A., and Saksman, E.: DRAM: Efficient adaptive MCMC, Stat Comput, 16, 339–354,

426 https://doi.org/10.1007/s11222-006-9438-0, 2006.

427

428 Hallet, B.: Glacial quarrying: a simple theoretical model, A. Glaciology., 22, 1–8,

429 https://doi.org/10.1017/S0260305500015147, 1996.

430

431 Hallet, B., Hunter, L., and Bogen, J.: Rates of erosion and sediment evacuation by glaciers: A review of field data

432 and their implications, Global and Planetary Change, 12, 213–235, https://doi.org/10.1016/0921-8181(95)00021-6,

433 1996.

434

435 Herman, F., De Doncker, F., Delaney, I., Prasicek, G., and Koppes, M.: The impact of glaciers on mountain erosion,

436 Nat Rev Earth Environ, 2, 422–435, https://doi.org/10.1038/s43017-021-00165-9, 2021.

437

438 Hogan, K. A., Jakobsson, M., Mayer, L., Reilly, B. T., Jennings, A. E., Stoner, J. S., Nielsen, T., Andresen, K. J.,

439 Nørmark, E., Heirman, K. A., Kamla, E., Jerram, K., Stranne, C., and Mix, A.: Glacial sedimentation, fluxes and

440 erosion rates associated with ice retreat in Petermann Fjord and Nares Strait, north-west Greenland, The Cryosphere,

441 14, 261–286, https://doi.org/10.5194/tc-14-261-2020, 2020.

442

443 Iverson, N. R.: Laboratory Simulations Of Glacial Abrasion: Comparison With Theory, J. Glaciol., 36, 304–314,

444 https://doi.org/10.3189/002214390793701264, 1990.

445

446 Iverson, N. R.: A theory of glacial quarrying for landscape evolution models, Geology, 40, 679–682,

447 https://doi.org/10.1130/G33079.1, 2012.

448

449 Joughin, I., Smith, B. E., Shean, D. E., and Floricioiu, D.: Brief Communication: Further summer speedup of

450 Jakobshavn Isbræ, The Cryosphere, 8, 209–214, https://doi.org/10.5194/tc-8-209-2014, 2014.

451

452 Kajanto, K., Seroussi, H., de Fleurian, B., and Nisancioglu, K. H.: Present day Jakobshavn Isbræ (West Greenland)
453 close to the Holocene minimum extent, Quaternary Science Reviews, 246, 106492,
454 https://doi.org/10.1016/j.quascirev.2020.106492, 2020.
455
456 Koppes, M. N.: Rates and Processes of Glacial Erosion, in: Treatise on Geomorphology, Elsevier, 169–181,
457 https://doi.org/10.1016/B978-0-12-818234-5.00032-8, 2022.
458
459 Koppes, M. N. and Montgomery, D. R.: The relative efficacy of fluvial and glacial erosion over modern to orogenic
460 timescales, Nature Geosci, 2, 644–647, https://doi.org/10.1038/ngeo616, 2009.
461
462 Krabbendam, M. and Glasser, N. F.: Glacial erosion and bedrock properties in NW Scotland: Abrasion and
463 plucking, hardness and joint spacing, Geomorphology, 130, 374–383,
464 https://doi.org/10.1016/j.geomorph.2011.04.022, 2011.
465
466 Matthes, Francois E.: Geologic history of the Yosemite Valley, US Geological Survey, 1930.
467 http://dx.doi.org/10.3133/pp160
468
469 Overeem, I., Hudson, B. D., Syvitski, J. P. M., Mikkelsen, A. B., Hasholt, B., van den Broeke, M. R., Noël, B. P. Y.,
470 and Morlighem, M.: Substantial export of suspended sediment to the global oceans from glacial erosion in
471 Greenland, Nature Geosci, 10, 859–863, https://doi.org/10.1038/ngeo3046, 2017.
472
473 Riihimaki, C. A.: Sediment evacuation and glacial erosion rates at a small alpine glacier, J. Geophys. Res., 110,
474 F03003, https://doi.org/10.1029/2004JF000189, 2005.
475
476 Ugelvig, S. V., Egholm, D. L., Anderson, R. S., and Iverson, N. R.: Glacial Erosion Driven by Variations in
477 Meltwater Drainage, J. Geophys. Res. Earth Surf., 123, 2863–2877, https://doi.org/10.1029/2018JF004680, 2018.
478
479 Weidick, A. and Bennike, O.: Quaternary glaciation history and glaciology of Jakobshavn Isbræ and the Disko Bugt
480 region, West Greenland: a review, GEUS Bulletin, 14, 1–78, https://doi.org/10.34194/geusb.v14.4985, 2007.
481
482 Weidick, A., Oerter, H., Reeh, N., Thomsen, H. H., and Thorning, L.: The recession of the Inland Ice margin during
483 the Holocene climatic optimum in the Jakobshavn Isfjord area of West Greenland, Global and Planetary Change, 2,
484 389–399, https://doi.org/10.1016/0921-8181(90)90010-A, 1990.
485
486 Young, N. E., Briner, J. P., Stewart, H. A. M., Axford, Y., Csatho, B., Rood, D. H., and Finkel, R. C.: Response of
487 Jakobshavn Isbrae, Greenland, to Holocene climate change, Geology, 39, 131–134,
488 https://doi.org/10.1130/G31399.1, 2011.

489

490    Young, N. E., Briner, J. P., Maurer, J., and Schaefer, J. M.: [10] Be measurements in bedrock constrain erosion

491    beneath the Greenland Ice Sheet margin, Geophys. Res. Lett., 43, https://doi.org/10.1002/2016GL070258, 2016.

492

493    Zoet, L. K., Alley, R. B., Anandakrishnan, S., and Christianson, K.: Accelerated subglacial erosion in response to

494    stick-slip motion, Geology, 41, 159–162, https://doi.org/10.1130/G33624.1, 2013.

495

496

497    **Figure captions**

498

499    **Figure 1.** A. Greenland. B. Jakobshavn region Aug 2018; extent of Jakobshavn Isbræ (J.I.) in 1850 CE;

500    J.If.=Jakobshavn Isfjord; nb/sb=north branch/south branch. C. Study area showing glacial erosion depths from

501    Balter-Kennedy et al. (2021) and this study (star). D. Oblique drone photograph of the study area (point of view

502    shown in C) showing study site A and B.

503

504    **Figure 2.** Photographs of surfaces in the study area. A) Heavily abraded and polished surface showing one of the

505    many "gouge trains;" view to SW. B) Small lee step (approximately 20 cm high) within a heavily abraded and

506    polished zone; note downflow from the lee cliff is a zone with more lightly abraded surfaces. C) Fresh surfaces with

507    minor grain-to-grain relief and limited evidence for abrasion shown within quarrying 'scars.' D) Focus on a lee step

508    (approximately 1 m high) showing the transition from a heavily abraded stoss surface (lightly colored) to darker-

509    colored, fresh lee faces; some of the dark color in this image is from subglacial precipitate "staining."

510

511    **Figure 3.** A) Study location A; blue area is extent of the quarried material. Stars are locations of [10]Be measurements.

512    B) Study location B; pair of quarried zones with a fresh, rough lee surface (left; sample ER2-A), and smooth,

513    abraded lee surface (right, sample ER2-B).

514

515    **Figure 4.** Concept model for [10]Be production and concentration for the field area. 1) Retreat of the ice sheet from

516    the field area 7.4 ka. Erosion during the last glaciation is sufficient to remove [10]Be to background levels. 2) The

517    paleo-surface is exposed to cosmic radiation during the Holocene until ice overrides at ~1790 CE, building up [10]Be

518    in the upper ~2 m of bedrock. 3) Ice readvances and erodes via abrasion and quarrying during the historical

519    advance. 4) The present-day surface is exposed in 2010 CE.

520

521

522    **Figure 5.** A) Photograph of Location A (see also Fig. 3A) showing fresh quarried face and floor. B) Cross section

523    representation of the 3D model domain for Location A. Sample locations are marked as black boxes. The red line

524    shows the present-day surface profile, while purple and green lines show rectangular and triangular pre-quarrying

525    surface profiles, respectively, used in forward model. The thin gray lines are the minimized surface profiles from the

526     MCMC inversion. C) Measured (small circles) and simulated (lines in color) [10]Be concentration of the three forward

527     model scenarios; colors match top.

528

529     **Figure 6.** A. Orthoimage of the field area showing fractures (blue lines) and lee cliff faces (red lines). Zones

530     quarried during the most recent glacial advance are outlined in purple. Rose diagram (inset) shows all measured ice

531     flow indicators (in the direction of ice flow). B. Elevation difference in quarried divots assigned to block removal

532     during the historical advance.

533

534     **Figure 7.** The orientation of ice-flow indicators subdivided into type. Blue lines encompass orientations from all

535     ice-flow indicators combined (see Fig. 6).

536

537     **Figure 8.** Photographs showing the relationship between crescentic gouges and quarrying at the field site. A) Gouge

538     trains leading to a lee face with evidence for quarried flakes initiated by a gouge process (ice flow from upper right

539     to lower left). B) Example of angled (and polished) lee face from which a relatively thin flake has been quarried and

540     removed.

541
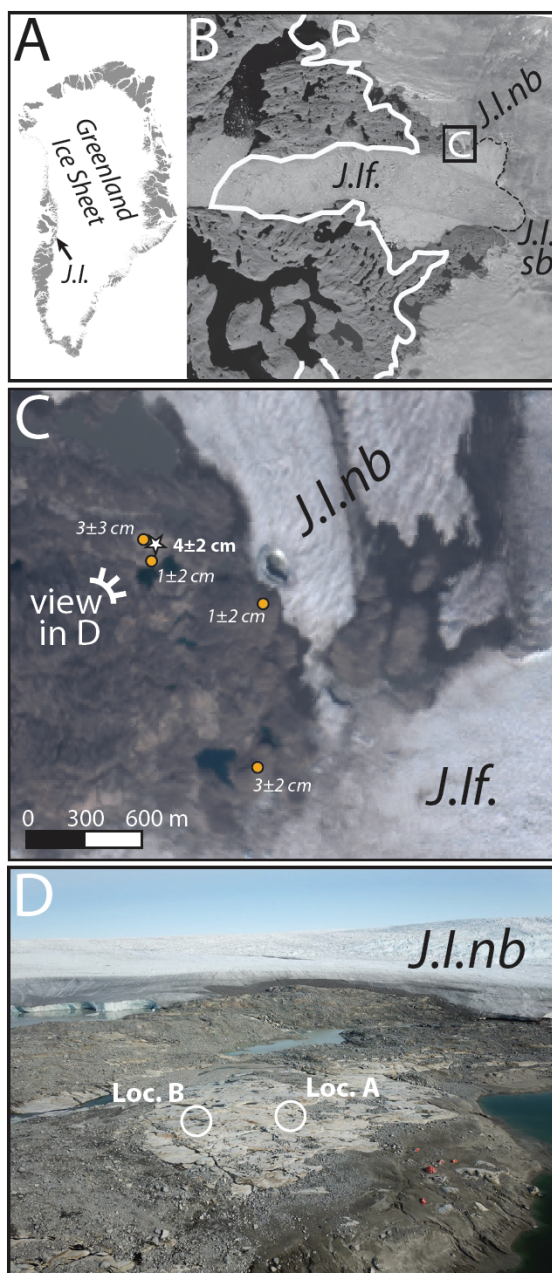
**Figure 1.** A. Greenland. B. Jakobshavn region Aug 2018; extent of Jakobshavn Isbræ (J.I.) in 1850 CE; J.If.=Jakobshavn Isfjord; nb/sb=north branch/south branch. C. Study area showing glacial erosion depths from Balter-Kennedy et al. (2021) and this study (star). D. Oblique drone photograph of the study area (point of view shown in C) showing study site A and B.
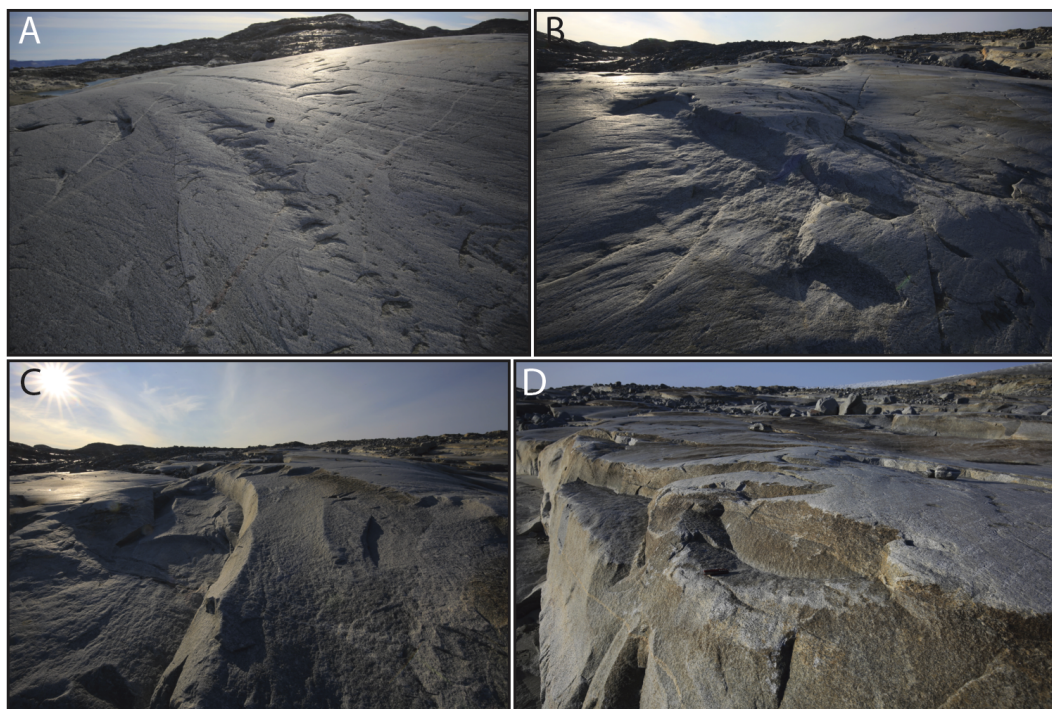
**Figure 2.** Photographs of surfaces in the study area. A) Heavily abraded and polished surface showing one of the many "gouge trains;" view to SW. B) Small lee step (approximately 20 cm high) within a heavily abraded and polished zone; note downflow from the lee cliff is a zone with more lightly abraded surfaces. C) Fresh surfaces with minor grain-to-grain relief and limited evidence for abrasion shown within quarrying 'scars.' D) Focus on a lee step (approximately 1 m high) showing the transition from a heavily abraded stoss surface (lightly colored) to darker-colored, fresh lee faces; some of the dark color in this image is from subglacial precipitate "staining."
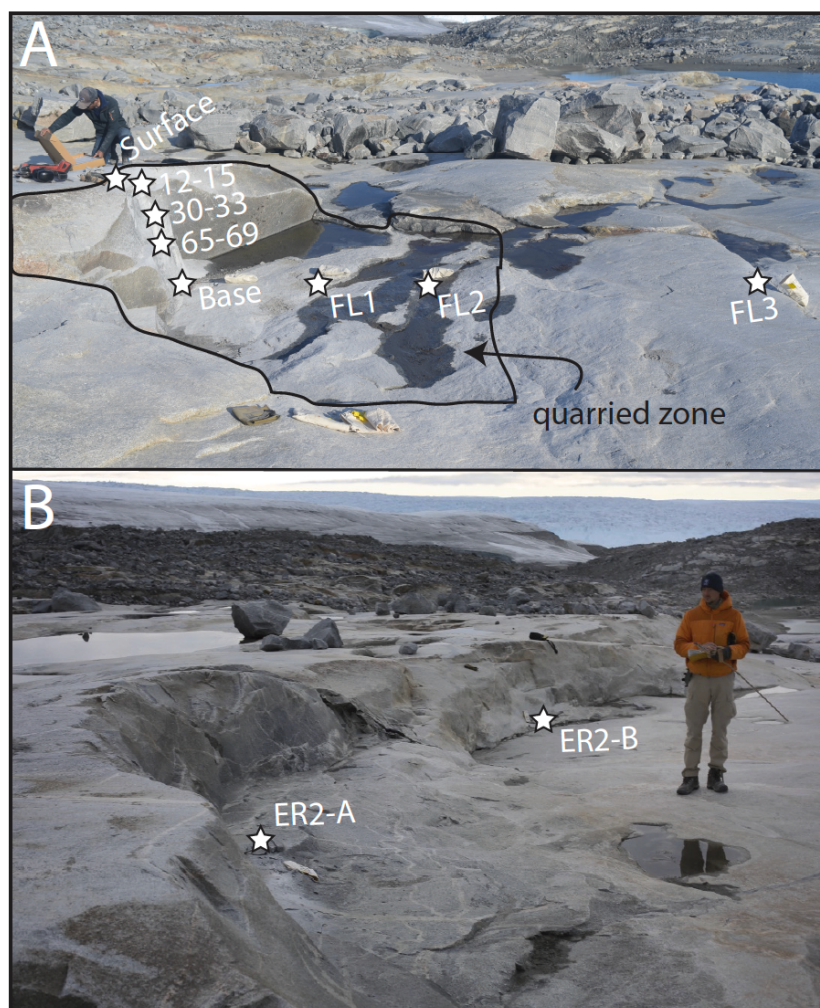
**Figure 3.** A) Study location A; blue area is extent of the quarried material. Stars are locations of $^{10}$Be measurements. B) Study location B; pair of quarried zones with a fresh, rough lee surface (left; sample ER2-A), and smooth, abraded lee surface (right, sample ER2-B).
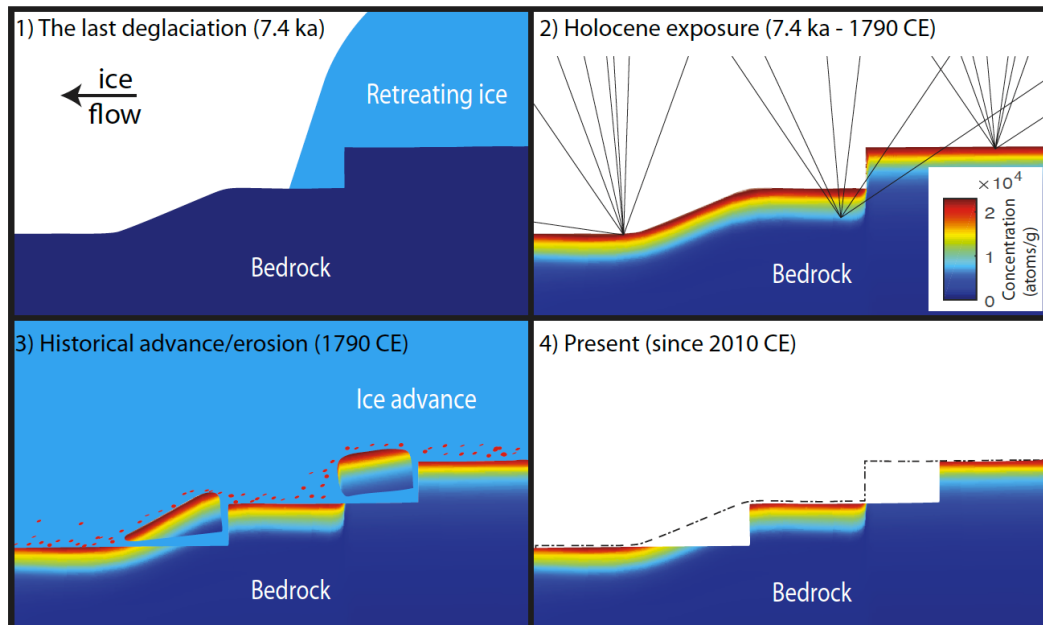
**Figure 4.** Concept model for [10]Be production and concentration for the field area. 1) Retreat of the ice sheet from the field area 7.4 ka. Erosion during the last glaciation is sufficient to remove [10]Be to background levels. 2) The paleo-surface is exposed to cosmic radiation during the Holocene until ice overrides at ~1790 CE, building up [10]Be in the upper ~2 m of bedrock. 3) Ice readvances and erodes via abrasion and quarrying during the historical advance. 4) The present-day surface is exposed in 2010 CE.
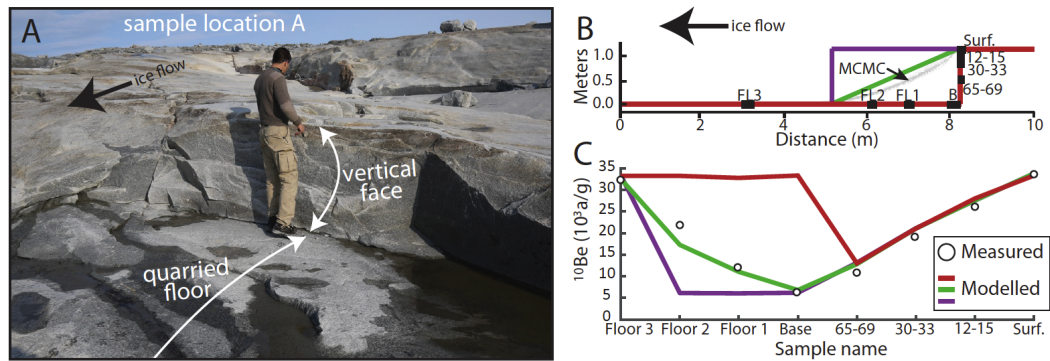
**Figure 5.** A) Photograph of Location A (see also Fig. 3A) showing fresh quarried face and floor. B) Cross section representation of the 3D model domain for Location A. Sample locations are marked as black boxes. The red line shows the present-day surface profile, while purple and green lines show rectangular and triangular pre-quarrying surface profiles, respectively, used in forward model. The thin gray lines are the minimized surface profiles from the MCMC inversion. C) Measured (small circles) and simulated (lines in color) $^{10}$Be concentration of the three forward model scenarios; colors match top.
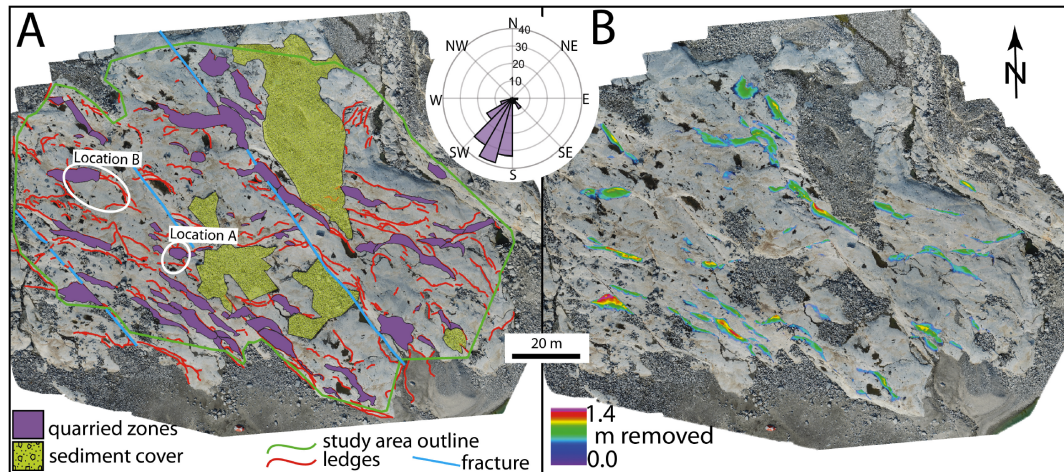
**Figure 6.** A. Orthoimage of the field area showing fractures (blue lines) and lee cliff faces (red lines). Zones quarried during the most recent glacial advance are outlined in purple. Rose diagram (inset) shows all measured ice flow indicators (in the direction of ice flow). B. Elevation difference in quarried divots assigned to block removal during the historical advance.
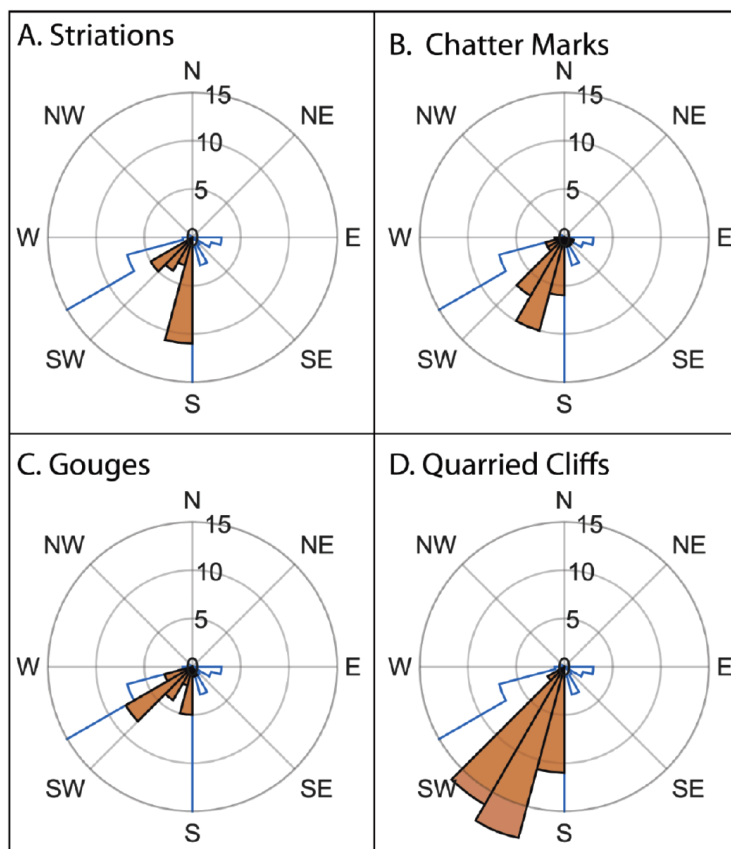
**Figure 7.** The orientation of ice-flow indicators subdivided into type. Blue lines encompass orientations from all ice-flow indicators combined (see Fig. 6).
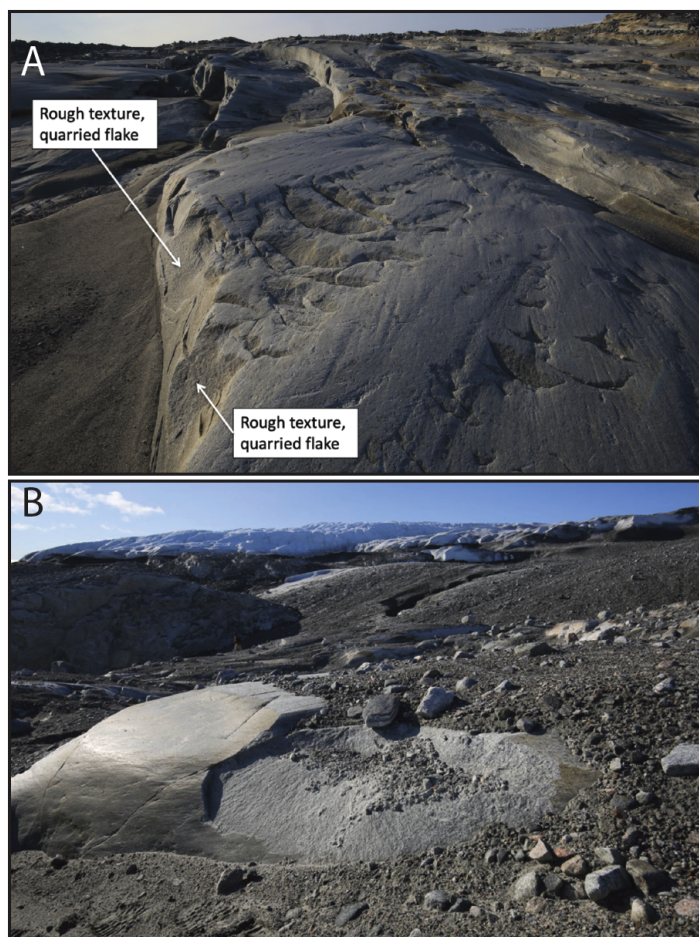
**Figure 8.** Photographs showing the relationship between crescentic gouges and quarrying at the field site. A) Gouge trains leading to a lee face with evidence for quarried flakes initiated by a gouge process (ice flow from upper right to lower left). B) Example of angled (and polished) lee face from which a relatively thin flake has been quarried and removed.

**Table 1.** MCMC parameters *a prior* and posterior.

| Parameter Name | Input | | | Output | |
| --- | --- | --- | --- | --- | --- |
| | Initial Guess | Minimum | Maximum | mean | std |
| xPoint | 0.6 | 0 | 1 | 0.70353 | 0.18268 |
| zPoint | 0.6 | 0 | 1 | 0.50464 | 0.22515 |
| Lambda (g cm$^{-2}$) | 208 | 150 | 240 | 184.26 | 12.518 |
| Abrasion Depth (cm) | 2.75 | 0 | 10 | 4.1375 | 1.9038 |

The *a priori* input into the MCMC inverse and the posterior output from the model runs that minimized the chi squared reduction.

**Table 2.** Beryllium-10 sample data.

| Sample Name | Qtz weight (g) | Carrier added (g) | $^{10}Be/^9Be$ (x10$^{-14}$) | Blank corrected $^{10}Be$ (atoms g$^1$) | Apparent Age (yr) |
| --- | --- | --- | --- | --- | --- |
| Surface | 56.821 | 0.1817 | 15.3±0.3 | 33,610±630 | 7,100±130 |
| 12-15 | 55.872 | 0.1822 | 11.7±0.2 | 26,090±490 | 5,510±100 |
| 30-33 | 60.139 | 0.1830 | 9.2±0.2 | 19,130±360 | 4,030±80 |
| 65-69 | 64.043 | 0.1818 | 5.5±0.1 | 10,730±240 | 2,260±50 |
| Base | 34.677 | 0.1820 | 1.8±0.1 | 6,210±210 | 1,310±40 |
| FL1 | 34.663 | 0.1832 | 3.3±0.1 | 11,910±320 | 2,510±70 |
| FL2 | 45.816 | 0.1835 | 8.0±0.2 | 21,870±500 | 4,630±110 |
| FL3 | 33.552 | 0.1832 | 8.5±0.2 | 31,940±570 | 6,740±120 |
| ER2-A | 26.190 | 0.1832 | 2.0±0.1 | 9,150±310 | 1,930±70 |
| ER2-B | 73.360 | 0.1834 | 14.6±0.3 | 25,090±480 | 5,300±100 |

Location A samples were located at 69.2316°N and 49.8093°W, and Location B samples (ER2) at 69.2318°N and 49.8103°W. All samples were at an elevation of 107 meters above sea level. Sample density was 2.65 g cm$^{-3}$, and the 07KNSTD Be standard was used. The Apparent Age is the St scaling apparent exposure duration, assuming no shielding.

**Table 3.** Eroded rock volume and glacial erosion rates

| | Volume (m$^3$) | Area. (m$^2$) | Rate (mm yr$^{-1}$) |
| --- | --- | --- | --- |
| Abrasion | 323±204 | 11,623* | 0.13±0.08 |
| Quarrying | 378±45 | 1843±208 | 0.13±0.03 |
| Total | 700±249 | 13,256 | 0.26±0.16 |

*value is 12% less than total area because of estimated area of subglacial cavities